Materials & Design 237 (2024) 112548

Contents lists available at ScienceDirect

Materials & Design

journal homepage: www.elsevier.com/locate/matdes

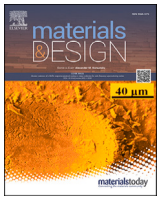

Minimal-surface-based multiphase metamaterials with highly variable stiffness

Xiaoyang Zheng [a], Ikumu Watanabe [a,*], Siqian Wang [b], Ta-Te Chen [c], Masanobu Naito [b]

[a] Center for Basic Research on Materials, National Institute for Materials Science, 1-2-1 Sengen, Tsukuba 305-0047, Japan
[b] Research Center for Macromolecules and Biomaterials, National Institute for Materials Science, 1-2-1 Sengen, Tsukuba 305-0047, Japan
[c] Graduate School of Engineering, Nagoya University, Furo-cho, Chikusa-ku, Nagoya 464-8603, Japan

ARTICLE INFO

Keywords:
Variable-stiffness materials
Mechanical metamaterials
Phase transition
Triply periodic minimal surfaces
Low-melting-point alloys
Shape memory

ABSTRACT

Variable-stiffness materials have a unique ability to change their stiffness reversibly in response to external stimuli or conditions. However, achieving ultrahigh stiffness change is often constrained by the geometric organization of the microstructures in most materials that exhibit variable stiffness. Therefore, to overcome this limitation, we introduce a metamaterial design inspired by triply periodic minimal surfaces for fabricating multiphase metamaterials. The specific geometric features of minimal surface designs facilitate interlocking bi- or tri-continuous interpenetrating phases such as air, resin, and alloy within a single multiphase metamaterial. These multiphase metamaterials are constructed by injecting a low-melting-point alloy (LMPA) into a 3D-printed elastic resin mold. The thermally-induced solid-liquid phase transition of the LMPA governs the stiffness change in multiphase metamaterials, ranging from Kilopascals to Gigapascals. Further contributing to this phenomenon, the superior resilience of the elastic resin enhances the shape-memory effect of the multiphase metamaterials. Applications of these materials in origami and deployable structures have been successfully demonstrated, highlighting their reconfigurability and volume compressibility. This innovative design strategy provides the foundation for crafting other metamaterials with intricately arranged internal phases. In conclusion, the proposed multiphase metamaterials have promising potential for various engineering applications where adaptability and morphing capabilities are essential.

1. Introduction

Variable-stiffness materials are characterized by a reversible transformation between a stiff, load-bearing state and a flexible, compliant state, allowing them to adapt to dynamical conditions [1]. This ability to change stiffness is widespread and can be observed in various phenomena such as the interaction of two contractile proteins in human skeletal muscle [2,3], regulation of the nervous system in sea cucumbers [4], and changes in microstructural porosity in plants [5,6]. In the field of artificial materials, variable stiffness can be accomplished through physical means (e.g., phase changes) and mechanical strategies (e.g., jamming), with the shape memory effect often manifesting through reversible transitions between rigid and soft states. Such features of variable stiffness and reversible shape transformation render these materials essential in diverse engineering fields, including shape morphing [7], actuators [8,9], soft robotics [10–13], biomedical devices [14], wearable electronics [15,16], and vehicles [17,18].

Synthetic materials such as metals, polymers, and magnetic fluids can switch between two phases to adjust their stiffness and other physical properties. For example, shape-memory alloys have a rigid state with Young's modulus (E) of approximately 1–100 GPa; however, their soft state is typically 2–4 times softer than the rigid state, leading to minimal stiffness variation and limited applications where flexibility is required [19]. In contrast, phase transitions in substances such as melting polymers, waxes, and metals enable an exceptionally large stiffness change ratio by reversibly switching between liquid and solid phases. Such transitions can be triggered by various factors, including temperature (e.g., low-melting-point alloys (LMPAs) and liquid crystal elastomers) [12,13,20–22], light (e.g., light-activated polymers) [23,24], moisture (e.g., polyurethane shape-memory polymers) [25], pH (e.g., pH-induced shape-memory polymers) [26], magnetic fields (e.g., magneto-rheological fluids) [27]. Proper encapsulation is often needed to contain the liquid state of melted materials for practical applications. Materials undergoing a glass transition, such as acrylonitrile

* Corresponding author.
E-mail address: WATANABE.Ikumu@nims.go.jp (I. Watanabe).

https://doi.org/10.1016/j.matdes.2023.112548
Received 5 October 2023; Received in revised form 16 November 2023; Accepted 3 December 2023
Available online 5 December 2023

butadiene styrene, polylactic acid (PLA), and polyethylene polymers, do not necessitate external hermetic encapsulation. However, they are relatively weak even in their rigid state, with their stiffness variation restricted to approximately 5–100× [28–30]. As a result, designing and fabricating materials that exhibit broad stiffness variations while maintaining the ability to bear substantial loads remains challenging.

A common strategy to realize broader stiffness variation and higher mechanical impedance involves using composite materials comprising a soft matrix and a rigid filler. LMPAs, which serve as desirable fillers for enhancing mechanical, thermal, and electrical properties [20,31], can be encapsulated in continuous structures such as meshes and scaffolds [32–34], or discontinuous forms such as particles [13,35,36], resulting in stiffness changes with a rigid-to-soft modulus ratio of up to 1500×. To prevent LMPA leakage, the volume fraction of LMPAs in these composites is generally kept below 55 vol.%. Compared to architected lattice counterparts, LMPA composites are consistently solid, hindering their applications where internal void spaces are necessary. While mechanical design strategies such as jamming and inflating can create delicately designed variable-stiffness materials with deployable microstructures, their stiffness change is relatively low (5–30×) compared to LMPA composites [37–41]. Hence, it remains a challenge to design the microstructure of LMPA composites to achieve remarkable stiffness variations and explore other unprecedented functionalities.

Mechanical metamaterials, characterized by repeating building blocks, display unique mechanical properties and functions and are shaped by the synergistic effects of the constituent materials and the geometric arrangements of the microstructures [42–47]. Unlike composites, where properties are customized by blending various components, mechanical metamaterials exert a more direct influence on each building block, resulting in unprecedented characteristics, such as ultrahigh strength-to-density ratios [48–50], negative Poisson's ratios [51–54], negative elastic moduli [55,56], near-zero shear moduli [57,58], deployable origami [59], and nonreciprocity [60]. The rapid advancements in deep learning and 4D printing technologies have significantly fueled the design and development of these mechanical metamaterials [42,61–63]. In particular, post-processing strategies, such as injecting stimulation-responsive materials into 3D-printed cavity structures, further enable obtaining programmable metamaterials [64]. The intricate design of metamaterial building blocks provides the foundation for tailoring the microstructures of LMPA composites to achieve remarkable variable stiffness. Based on this idea, LMPA metamaterials were fabricated by filling liquid metals into 3D-printed elastomer lattices [65,66]. However, these lattice microstructures were not optimized in terms of mechanical properties and geometrical features, resulting in less stiffness variations.

Bi-continuous interpenetrating matrix/filler structures present a promising pathway to enhance the filler volume ratio and stiffness. These structures are found in spinodal topologies and triply periodic minimal surfaces (TPMSs) [67–70]. Unlike spinodoid metamaterials, which consist of disordered microstructures generated by simulating spinodal phase separation, TPMS-based metamaterials possess ordered microstructures with crystalline symmetry and smooth surfaces, leading to superior mechanical attributes [67,71]. Additionally, the chiral symmetry of TPMS-based metamaterials allows for twin skeletons separated by a sheet interface, facilitating the creation of multiphase metamaterials [72,73]. The TPMS topologies, being mathematically defined by implicit functions, can be readily generated using computational tools such as MATLAB or Python codes [74]. This mathematical modeling approach and the geometric features of TPMSs position them as promising candidates for variable-stiffness materials.

In this study, we introduced tri-continuous multiphase (air, elastic resin, and LMPA) metamaterials—which exhibit highly variable stiffness—derived from TPMSs. Compared with LMPA composites and lattice-based LMPA multiphase metamaterials [65,66], the TPMSs-based interpenetrating microstructure enables encapsulating a higher volume fraction of LMPA in the metamaterials, and its topological features also enable more homogeneous stress distribution [71]. The resin phase separates the air and LMPA phases in these structures. We generated the geometries of the multiphase metamaterials with arbitrary volume fractions using implicit functions, and subsequently 3D printed samples using a rubber-like elastic resin, filled later with an LMPA. We then examined their mechanical properties through temperature-dependent mechanical tests and corroborated the findings using finite element method (FEM) simulations. Our demonstration of encapsulating continuous LMPA within TPMSs led to multiphase metamaterials capable of ultrahigh stiffness changes—up to 10^5×—as they transitioned from a stiff to a soft state through LMPA melting induced by heating. Finally, we highlighted their potential applications in origami and deployable structures, emphasizing their practical relevance and adaptability.

2. Methods

2.1. Modeling

A TPMS represents a smooth surface with zero mean curvature and cubic symmetry. Common TPMSs encompass structures such as the gyroid, Schwarz diamond, and Schwarz primitive. These structures can be mathematically expressed using an implicit function corresponding to the level-set approximation equation. The isosurfaces for the three topologies are defined as:

$$F(\text{Gyroid}) = \cos x \sin y + \cos y \sin z + \cos z \sin x + t \tag{1}$$

$$F(\text{Diamond}) = \sin x \sin y \sin z + \sin x \cos y \cos z + \cos x \sin y \cos z + \cos x \cos y \sin z + t \tag{2}$$

$$F(\text{Primitive}) = \cos x + \cos y + \cos z + t \tag{3}$$

where the level-set parameter t functions as a variable controlling the volume fractions of the two phases separated by the TPMS isosurface, illustrated in Fig. 1. When $t = 0$, the isosurface partitions the domain into bi-continuous phases exhibiting chiral symmetry. As depicted in Fig. 1d, the volume fraction of the two bi-continuous phases varies with t, enabling tuning the maximum and minimum stiffnesses within multiphase metamaterials. While the volume fraction of the phase in the normal direction follows a linear relationship with t within these TPMS isosurfaces, the phase may fragment into isolated blobs in the primitive isosurface for $t < -1$. Notably, a cubic domain may be segmented into three tri-continuous phases using two isosurfaces with different t values or even more interpenetrating phases with additional isosurfaces (Figs. 1a–c). This segmentation results in dual-phase metamaterials, where soft and rigid phases are demarcated by isosurfaces, or a triphase metamaterial consisting of air, soft, and rigid phases, where the soft phase occupies the region between the two isosurfaces, separating the other components.

An isosurface of the TPMS topology was generated based on an implicit function using MATLAB (MathWorks, USA). Next, this isosurface was automatically imported into an FEM simulation platform (COMSOL Multiphysics Ver. 6.0, COMSOL, Sweden) via the LiveLink interface. This interface facilitated the adjustment of volume fractions and the execution of geometric operations. The resultant geometry could be directly utilized for FEM simulations or exported as an STL file for 3D printing. The exported STL file was further modified using CAD software (3Ds max, Autodesk, USA) to capture unnecessary open boundaries, then sliced using PreForm (Formlabs, USA) before 3D printing.

2.2. Samples preparation

The design and fabrication process of LMPA-filled multiphase metamaterials were illustrated in Fig. 2. Each specimen of the multiphase metamaterial, consisting of 3×3×3 unit cells with length size of 30 mm, was prepared using the injection molding method. Initially, a rubber-like mold was 3D printed with an elastic photopolymer resin (Elastic

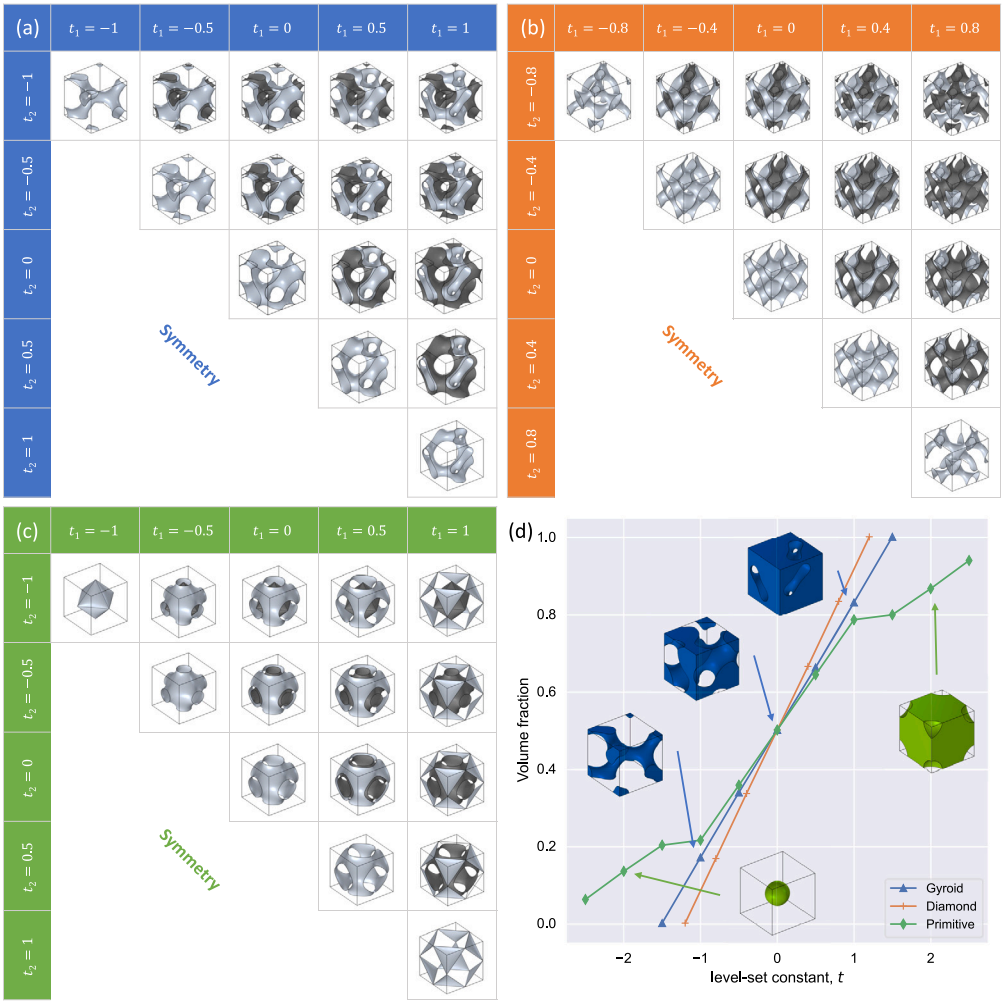

Fig. 1. TPMSs for designing multiphase metamaterials. (a–c) Isosurfaces of three TPMSs: Gyroid (a), Diamond (b), and Primitive (c). Isosurfaces can shrink and expand with a change of level-set parameter t. Cubic domain can be divided into two phases using one isosurface or three phases using two isosurfaces with different t. (d) Volume fraction versus level-set parameter t. Volume fraction of phase in a normal direction of isosurface shows a linear relationship with t. The cubic domain could be segmented into unconnected blobs in a Primitive isosurface where $t < -1$ or $t > 1$.

50A resin, Formlabs, USA) and a 3D printer (Form 3, Formlabs, USA), with layer thickness set to 0.05 mm. No additional support structures were used in the 3D printing process to ensure a refined surface finish. The completed 3D-printed mold was washed with isopropanol for 10 min, then cured at 60 °C for 20 min using Form Cure (Formlabs, USA). 20 min is the recommended post-curing time for Elastic 50A Resin, which ensures that the 3D-printed parts reach their optimal mechanical properties. Subsequently, the mold was filled by injecting a melted LMPA, which had been heated with boiling water. The LMPA is lead- and cadmium-free LMPA and composed of 57 wt% Bismuth, 17 wt% Tin, and 26 wt% Indium. The LMPA-filled mold underwent degassing in a polycarbonate desiccator at 100 °C under high-vacuum conditions for 30 min. After cooling, the open boundaries of the LMPA-filled mold were sealed with elastic resin, followed by a final curing process. Specimens with different phase volume fractions are represented by R_iA_j, where i is the volume fraction of the resin and j is the volume fraction of the alloy. For specimen $R_0A_{0.5}$, the resin was removed mechanically by hand.

2.3. DSC test

Thermal analysis of both LMPA and elastic resin was conducted utilizing a Differential scanning calorimetry (DSC) test (DSC-60, Shimadzu, Japan). A test sample weighing approximately 10 mg was placed inside an aluminum pan equipped with a pierced lid. The sample was heated to 150 °C, maintained at that temperature for 10 min, and then cooled to 0 °C. It was repeated for two continuous thermal cycles. The scanning rate and the nitrogen flow were set at 10 °C/min and 100 mL/min, respectively.

2.4. Microindentation test

Elastic modulus of LMPA at room temperature was measured by microindentation tests using TI950 triboindenter (Bruker Co., USA) equipped with a high-load module and a Berkovich indenter. Before testing, the LMPA samples were meticulously mechanically polished. The maximum indentation load was predetermined at 1.5 N, with a holding time of 20 s and the loading and unloading rates uniformly set to 0.1 N/s. These indentation tests were conducted 50 times to ensure accuracy, with average values considered to mitigate any potential experimental errors. The indentation hardness and elastic modulus was evaluated using the load–displacement curve obtained from the indentation test, employing the Oliver–Pharr method for the calculations [75–78].

2.5. Compression test

The mechanical properties of the multiphase metamaterial specimens were examined using uniaxial compression tests conducted on

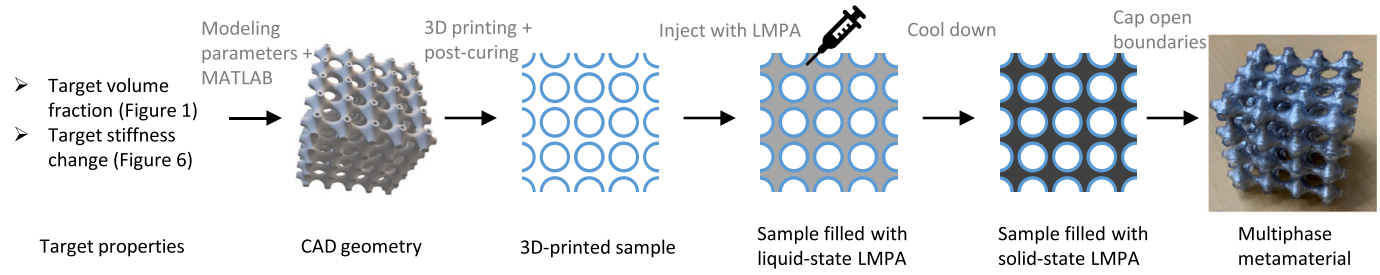

Fig. 2. Design and fabrication process of LMPA-filled multiphase metamaterials. A multiphase metamaterial with target volume fraction or stiffness change can be retrieved according to volume fraction–level-set parameter curves and stiffness contour maps, respectively. Given modeling parameters (i.e., implicit function and level-set parameters), a CAD geometry is generated using MATLAB code. The CAD geometry is sliced and then printed by a 3D printer, followed by washing and post-curing. The 3D-printed sample is injected with liquid LMPA in a 100 °C chamber. A multiphase metamaterial is prepared after cooling and capping the open boundaries using elastic resin.

a motorized test stand (AG-Xplus-10kN, Shimadzu, Japan). These tests were conducted at a constant displacement rate of 1 mm/min. Throughout the testing, the load and displacement data were carefully recorded, creating stress–strain curves. The Young's moduli of the specimens were determined by linearly fitting the data within the initial linear elastic region, and the yield strengths were computed utilizing the 1% offset stress method. Additionally, high-temperature examinations were performed inside a thermostatic chamber (TCE-N300, Shimadzu, Japan). For these tests, the specimens were first preheated to 100 °C and maintained at this temperature for 10 min before the loading process commenced.

2.6. FEM simulations

The mechanical properties of the multiphase metamaterials were extensively and quantitatively analyzed using FEM simulations (COMSOL Multiphysics Ver. 6.0, COMSOL, Sweden). In the simulations conducted at room temperature, the elastic resin was characterized using an incompressible neo-Hookean model with Young's modulus of 0.6615 MPa; while the LMPA was characterized using a compressible neo-Hookean model with Young's modulus of 53.47 GPa based on the equivalent Young's modulus measured by the microindentation test and an assumption that the Poisson's ratio is 0.3, and an isotropic perfectly plasticity model. The yield strength of the LMPA was determined as 738 MPa by minimizing the difference between the experimental and computational results of compression tests in the multiphase metamaterial specimens. The elastic resin model remained unchanged during high-temperature simulations, but the LMPA was modeled as a liquid material which is an incompressible low stiffness material using an incompressible neo-Hookean model with Young's modulus of 1 Pa. To ensure both computational efficiency and accuracy, the geometries were meshed using approximately 2×10^5–3×10^5 second-order tetrahedral solid elements. The simulations were conducted using the representative volume element technique, employing a parametric sweep of the displacement along the z-axis and applying periodic boundary conditions [79,80]. These FEM simulations generated the macroscopic stress–strain curves corresponding to the compression tests and the Young's moduli of the multiphase metamaterials.

3. Results and discussion

3.1. Material design strategy

To achieve a broad spectrum of stiffness variation, the design must incorporate a rigid phase capable of reversible transition between melting and solid states upon mild stimuli, a soft phase that is sufficiently robust and resilient to encapsulate the rigid phase, and a significant stiffness disparity between the soft and rigid phases. Additive manufacturing and injection molding were employed to fabricate the designed

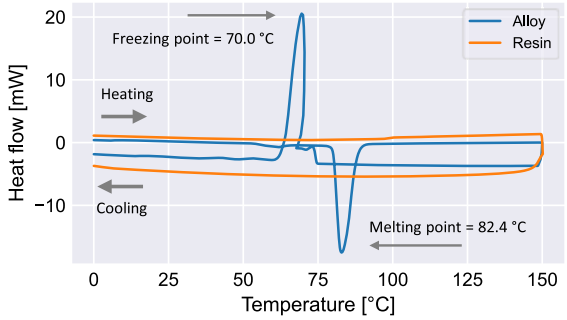

Fig. 3. DSC curves of low-melting-point alloy and elastic resin.

multiphase metamaterials. For optimal surface finish, elasticity, and resilience, the soft phase was 3D printed as a mold utilizing rubber-like elastic resin via stereolithography (SLA) technology. This elastic resin is modeled as an incompressible neo-Hookean solid with Young's modulus of 0.6615 MPa [51]. The rigid phase was selected as a LMPA as it has adequate Young's modulus and melting pointing. The LMPA exhibits Young's modulus of 53.47 GPa as determined through microindentation tests. DSC analysis reveals the LMPA's melting point to be approximately 82.4 °C, while the elastic resin lacks any discernible melting or glass transition within the 0–150 °C range (Fig. 3). This property enables the multiphase metamaterial composed of LMPA and resin to significantly soften upon heating and retain its deformed shape after cooling.

To demonstrate the feasibility of creating such multiphase metamaterials, we utilized 3D printing to fabricate five distinct gyroid topologies, each with different volume fractions, using a rubber-like elastic resin. These resin molds encapsulated the LMPA, which was subsequently melted and injected into the molds. While preparing these multiphase metamaterials, the open boundaries of the LMPA phase were carefully captured while preserving the air phase. The resin framework could be mechanically removed for a pure gyroid topology consisting solely of LMPA. Fig. 4a compares the renderings and the actual specimens of the multiphase metamaterials, showcasing variations in volume fractions. The structure of each multiphase metamaterial sample is composed of $3 \times 3 \times 3$ unit cells. Additionally, the outer boundaries of the LMPA phases within the specimens were covered in a thin layer of resin, providing a well-defined and intricate structural design. However, some bubbles are observed in the prepared samples, implying that the LMPA phase does not fully fill the blank channels, as shown in Fig. 4b. The surface of LMPA is relatively rough, which attributes to the surface finish of the SLA 3D printing technique (Fig. 4b). The bubble problem can be alleviated using a longer degassing time, and the surface roughness can be improved using a higher-resolution 3D printing technique, such as projection micro-stereolithography 3D printing [65,81].

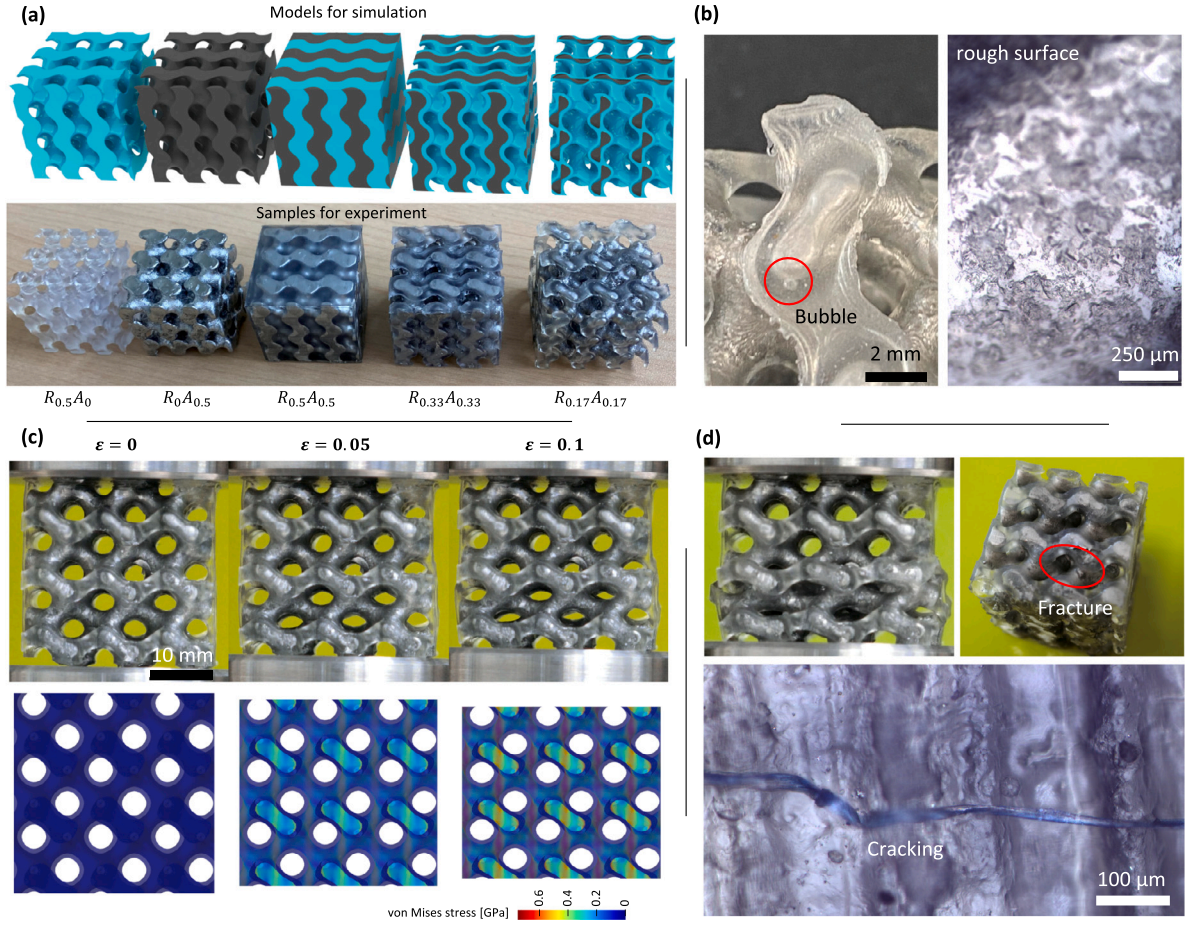

Fig. 4. Multiphase metamaterials with different volume fractions. (a) Renderings and specimens of multiphase metamaterials derived from Gyroid topology. Multiphase metamaterials with different phase volume fractions are represented by R_iA_j, where i is the volume fraction of the resin and j is the volume fraction of the alloy. Multiphase metamaterials with higher ratios of LMPA can also be prepared using structures shown in Fig. 1. (b) Defects of prepared samples, showing bubbles (left) and rough surface (right). (c) Sequence of progressively deformed configurations of the specimen, $R_{0.17}A_{0.17}$. (d) A sample after large deformation, suffering from structural failure (upper left), resin fracture (upper right), and cracking in LMPA (bottom).

3.2. Mechanical properties

The mechanical behavior of the specimens was explored using uniaxial compression tests at both room temperature and 100 °C. Fig. 4c shows a sequence of progressively deformed shapes of the specimen, $R_{0.17}A_{0.17}$, under three different levels of longitudinal engineering strain within $\varepsilon < 0.1$. Fig. 4c also shows corresponding simulation results, where the von Mises stress concentrates along loading direction and form a series of vertically continuous helix ribbons. The specimen witnesses a typical deformation of porous materials without clear fracture or crack, attributing to its optimized topology compared with other lattice-based structures [68,71]. However, the LMPA would crack when undergoing larger deformation, as shown in Fig. 4d where $\varepsilon = 0.25$. Also, the fracture of resin will also happen at large deformations because of the lower ultimate tensile strength (3.32 MPa) and tear strength (19.1 kN/m) of the resin. Fig. 4d also shows another specimen, $R_{0.33}A_{0.33}$, cracking in its resin surface after a large deformation of $\varepsilon = 0.2$. To alleviate fracture and crack, the resin boundary should be thicker and large deformation should be avoided.

Fig. 5a illustrates the experimental stress–strain curves from the tests conducted at room temperature, visually represented as ribbons. Each ribbon encompasses the area between the lines from three separate uniaxial compression tests performed on a single specimen. These stress–strain curves display the standard characteristics of plastic deformation, consisting of an initial linear elastic region followed by a plastic plateau. Young's moduli of the specimens were determined by linearly fitting the elastic region, while the yield strengths were identified as the 1% offset stress within the stress–strain curves. As written in Section 2.6, the yield strength of the LMPA was calculated based on the stress–strain curves of compression tests of the multiphase metamaterial specimens. At room temperature, the stiffness and strength of these multiphase metamaterials are primarily due to the LMPA, which behaves as a solid and robust material. However, when subjected to temperatures 100 °C above the melting point of LMPA, these metamaterials become considerably softer, exhibiting altered deformation behavior as depicted in Fig. 5b. In this state, the stress–strain curves remained linear within a 10% engineering strain during compression, resulting in the Young's moduli ranging from approximately 50–300 kPa.

FEM simulations were conducted to corroborate the experimental findings and determine the mechanical characteristics of both LMPA and the elastic resin. Fig. 4a presents the geometric models employed in the FEM analysis, including two or three constitutive material components (LMPA, elastic resin, and air) equipped with temperature-dependent parameters. The slight difference between simulation and experimental results came from the surface finish and uncured surface of 3D printed samples, the bubbles of residual air inside the samples, the partially oxidized LMPAs, and the different boundary conditions. These simulation outcomes showed strong alignment with the experimental results at both room temperature and 100 °C (Figs. 5a and b), thereby confirming the precision and effectiveness of the FEM model in replicating real-world behavior.

We further analyzed Young's moduli of these multiphase metamaterials at room temperature and 100 °C, with the results depicted in

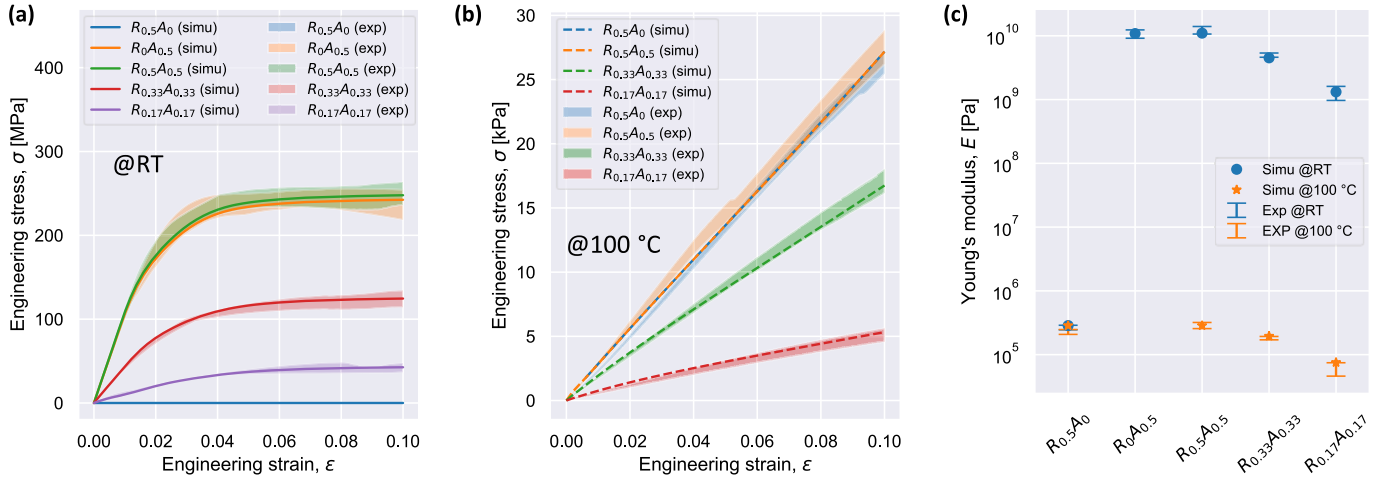

Fig. 5. Mechanical properties of multiphase metamaterials with different volume fractions. (a,b) Stress–strain curves from uniaxial compression tests and FEM simulations at room temperature (d) and 100 °C (e). (c) Young's moduli of these multiphase metamaterials at room temperature and 100 °C.

Fig. 5c. For the specimen designated as $R_{0.5}A_0$, Young's moduli exhibited negligible change between the two temperatures, substantiating that the elastic resin's properties remain stable within 25–100 °C temperature range. In contrast, the other specimens demonstrated a pronounced alteration in stiffness: their Young's moduli decreased sharply from approximately 1.99 GPa, 6.66 GPa, and 13.4 GPa at room temperature to 3.79×10^{-5} GPa, 1.11×10^{-4} GPa, 1.76×10^{-4} GPa at 100 °C for $R_{0.33}A_{0.33}$, $R_{0.17}A_{0.17}$, and $R_{0.5}A_{0.5}$, respectively. This transformation in stiffness reaches an ultrahigh factor of $10^5\times$, a performance that outshines most materials with variable stiffness achieved through different mechanisms, such as glass transition [28–30,82–84], jamming [38–41], and melting [13,24,32–36,85–87], as illustrated in Fig. 6.

The extraordinary shift in stiffness within the proposed multiphase metamaterials is predominantly governed by the melting process, where the phase transition of the LMPA from liquid to solid markedly boosts stiffness and strength. Unlike other materials where melting is the dominant factor affecting stiffness variability, the exceptional stiffness transformation in the multiphase metamaterials can be attributed to specific geometric attributes. A two-phase metamaterial is characterized by bi-continuous interpenetrating phases (i.e., LMPA and resin), while a three-phase metamaterial includes tri-continuous interpenetrating phases (i.e., LMPA, resin, and air). However, in the most melting-governed variable-stiffness materials, LMPAs are typically encapsulated in either discontinuous forms, such as particles and flakes, or nontopological forms, such as meshes and scaffolds [13,32–36]. This encapsulation often leads to comparatively lower shifts in the rigid-to-soft modulus ratio. Although certain ionogel based on glass transition can achieve a remarkable stiffness change ratio of up to 1.1×10^5 [83], their maximum attained Young's modulus (85 MPa) is remarkably low as comparison with that exhibited by multiphase metamaterials (53.47 GPa).

Given the remarkable qualitative and quantitative alignment between the experimental results and FEM simulations, we further investigated the impact of the volume fractions of the three phases (i.e., LMPA, resin, and air) on the stiffness of the TPMS-based multiphase metamaterials using FEM models. As the level-set parameter t can easily adjust the volume fraction of each phase, we conducted a parametric study by integrating MATLAB with COMSOL Multiphysics. MATLAB generated multiphase metamaterial geometries through implicit functions, while COMSOL Multiphysics was used to perform FEM simulations. Fig. 7 illustrates the stiffness maps of the multiphase metamaterials created from the three distinct TPMS topologies. Each map, containing 28 data points, was generated through 2D contour plotting. The locations corresponding to the gyroid topology specimens utilized in the experiments are specifically marked in Fig. 7, spanning a broad area within the data map. For all three categories of TPMS topology-based multiphase metamaterials, the stiffness maps at room temperature displayed a consistent pattern: their Young's moduli were primarily determined by the volume fraction of the LMPA and were only marginally affected by the other two phases. The Young's moduli ranged from 0 Pa (when occupied entirely by the air) phase to 53.47 GPa (when filled with LMPA). Conversely, Young's moduli at 100 °C were considerably influenced by the volume fraction of the rubber phase, increasing from 0 Pa to 0.6625 MPa when filled with the resin phase. The slight discrepancy between the primitive topology and the other two topologies within the stiffness maps can be attributed to isolated blobs in the primitive topology at low volume fractions, as depicted in Fig. 1d. These stiffness maps effectively demonstrate that multiphase metamaterials can achieve a diverse range of Young's moduli, allowing for tunable stiffness.

To elaborate the relationship between structural types, stiffness variation, and multiphases of these multiphase metamaterials, we further build the scaling laws of relative Young's modulus following the Gibson–Ashby model [90]. As the stiffness of these multiphase metamaterials is dominated by the volume fraction of the LMPA phase at room temperature and the resin phase at 100 °C, respectively, the scaling laws of these topologies are fitted according to the temperature. At room temperature, the effective Young's moduli of these multiphase metamaterials can be estimated by fitting the data from Figs. 7a–c:

$$E^{\text{room}}_{\text{Gyroid}} = E_{\text{alloy}} \times 0.9769\rho^{1.968}_{\text{alloy}}, R^2 = 0.9989 \quad (4)$$

$$E^{\text{room}}_{\text{Diamond}} = E_{\text{alloy}} \times 0.9935\rho^{1.906}_{\text{alloy}}, R^2 = 0.9998 \quad (5)$$

$$E^{\text{room}}_{\text{Primitive}} = E_{\text{alloy}} \times 0.9963\rho^{2.291}_{\text{alloy}}, R^2 = 0.9997 \quad (6)$$

Similarly, at 100 °C, the effective Young's moduli can be fitted according to Figs. 7d–f:

$$E^{100\,^\circ\text{C}}_{\text{Gyroid}} = E_{\text{resin}} \times 0.9675\rho^{1.808}_{\text{resin}}, R^2 = 0.9955 \quad (7)$$

$$E^{100\,^\circ\text{C}}_{\text{Diamond}} = E_{\text{resin}} \times 0.9819\rho^{1.761}_{\text{resin}}, R^2 = 0.9977 \quad (8)$$

$$E^{100\,^\circ\text{C}}_{\text{Primitive}} = E_{\text{resin}} \times 0.9798\rho^{1.900}_{\text{resin}}, R^2 = 0.9885 \quad (9)$$

where $E_{\text{alloy}} = 53.47$ GPa and $E_{\text{resin}} = 0.6615$ MPa are the Young's moduli of the LMPA and the resin, respectively. ρ_{alloy} and ρ_{resin} are the volume fractions of the LMPA and the resin, respectively. Consequently, for a multiphase metamaterial with given volume fractions of each phase, its effective Young's moduli at room temperature and 100 °C can be estimated by the Equations (4)–(9).

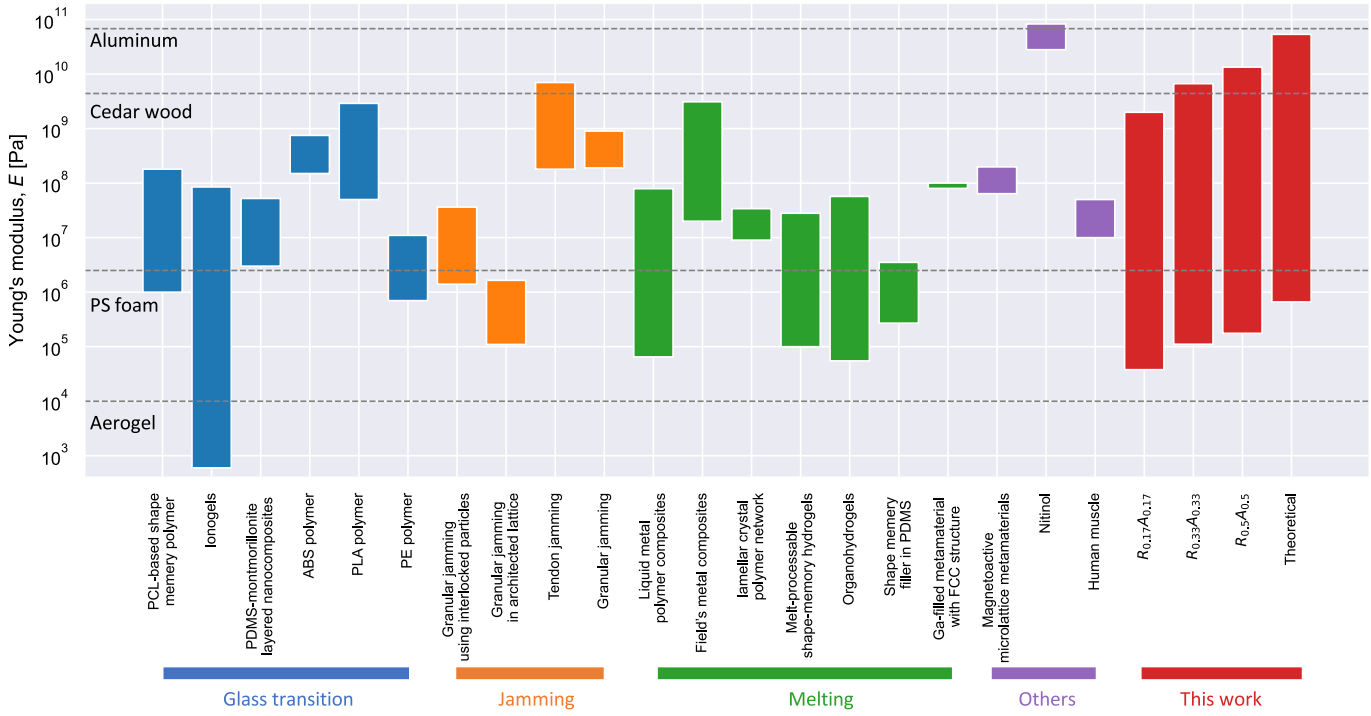

Fig. 6. Stiffness change of multiphase metamaterials and other variable-stiffness materials. Melting-based multiphase metamaterials show high stiffness change among others. The theoretical one represents the highest and lowest Young's moduli of a solid cube, i.e., LMPA and resin cubes. Different variable stiffness mechanisms have been compared in this figure, including glass transition mechanism: polycaprolactone (PCL)-based shape-memory polymer [82], ionogels [83], polydimethylsiloxane (PDMS)-montmorillonite layered nanocomposites [84], Acrylonitrile butadiene styrene (ABS) [28], polylactic acid (PLA) [29], and polyethylene (PE) [30]; jamming mechanism: granular jamming using interlocked particles [38], granular jamming in architected lattices [39], tendon jamming [40], and granular jamming [41]; melting mechanism: liquid metal-polymer composites [34], Field's metal composites [13], lamellar crystal polymer network [85], melt-processable shape-memory hydrogels [86], organohydrogels [87], shape-memory filler in PDMS [24], and Ga-filled metamaterial with FCC structure [65]; and others: magnetoactive microlattice metamaterials [81], nitinol [88] and human muscle [89].

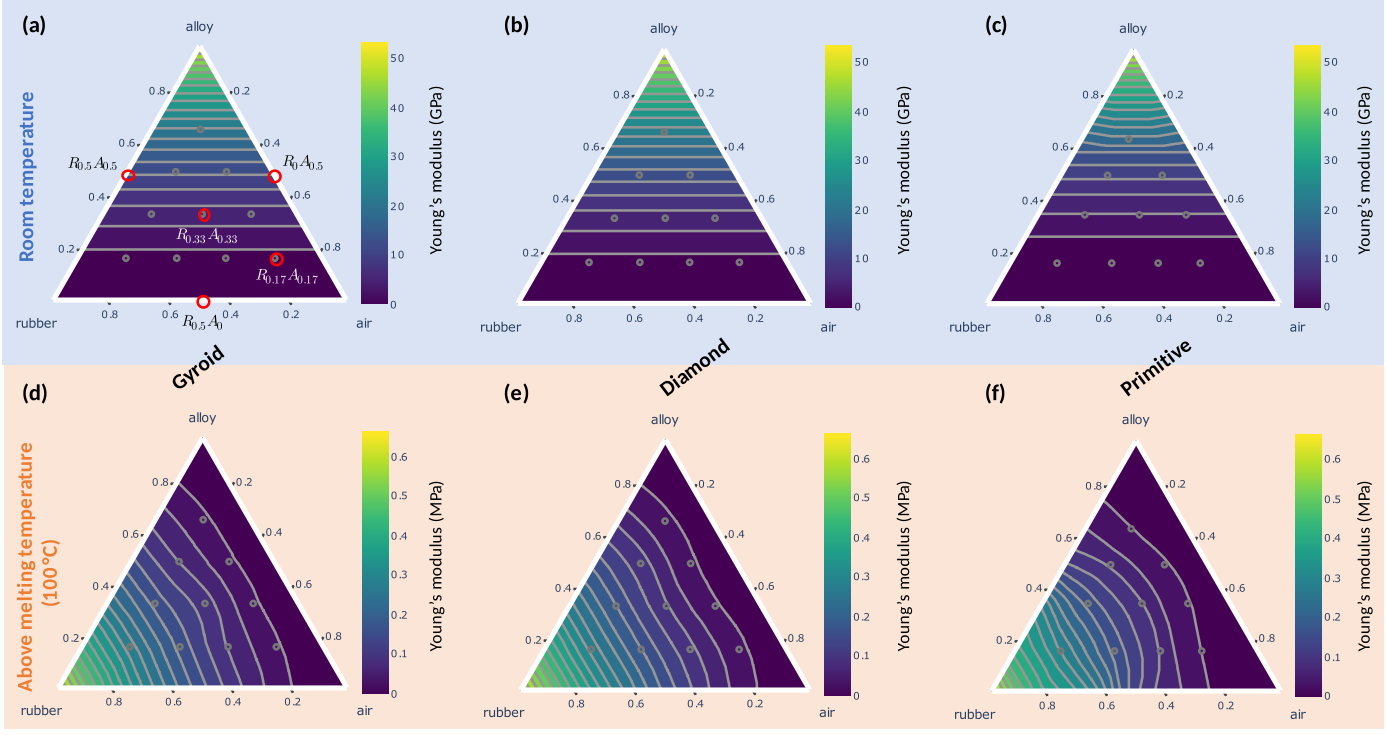

Fig. 7. Stiffness map of multiphase metamaterials based on three TPMS topologies. The values of parameter t in each were chosen from Fig. 1, where each type of TPMS geometry has 25 different pairs of t values. Each contour map was plotted using the 25 multiphase metamaterials and 3 pure phases (i.e., alloy, rubber, and air), i.e., 28 geometries with different volume fractions. (a) Gyroid, (b) Diamond, (c) Primitive at room temperature; (d) Gyroid, (e) Diamond, (f) Primitive at 100 °C.

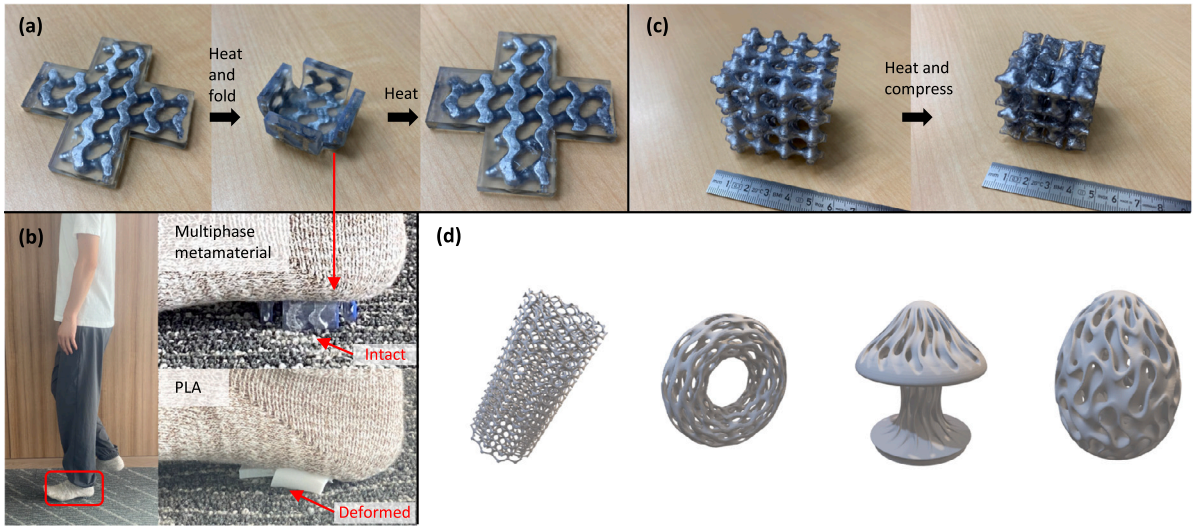

Fig. 8. Applications of multiphase metamaterials. (a) Origami structure based on a multiphase metamaterial. Unfolded cube net made of multiphase metamaterial can be folded into a cube while keeping the deformed state; it will recover to its original shape when heated again. (b) Folded multiphase metamaterial cube can bear an adult's weight without any deformation, but a folded PLA cube deformed and bent. (c) Deployable structure based on multiphase metamaterials. It can shrink under uniaxial compressive load after heated. (d) Gallery of multiphase metamaterials based on TPMS topologies, including a hollow cylinder, torus, mushroom, and egg.

3.3. Applications

To highlight the benefits of the proposed multiphase metamaterials, we designed both an origami structure and a deployable structure, showcasing the exceptional variable stiffness and intricate geometrical topological microstructure, respectively. Origami structures and deployable structures are associated with "foldable" and "deployable", respectively. They are potential candidates in aerospace engineering and architectural engineering, such as small satellites and portable houses [91,92]. In these multiphase metamaterials, the significant change in stiffness grants them enhanced load-bearing capacity, while the porous microstructure allows them to alter their configuration through folding and deploying. We crafted an origami structure (specifically, an unfolded cube net) measuring 20 mm in length and 4 mm in thickness, as depicted in Fig. 8a. The structure was fabricated by injecting LMPA into a 3D-printed elastic resin mold. Fig. 8a illustrates transforming the unfolded cube net into a cube by heating and softening it with boiling water. As the melting temperature of LMPA is approximately 82.4 °C, the cube net can be softened and made deformable by immersing it in hot water. Once heated beyond its melting temperature, the cube net can be easily folded, with the deformed shape remaining intact upon cooling. Remarkably, owing to the residual stresses in the elastic resin, the folded cube spontaneously reverted to its original shape when reheated above the melting temperature, further evidencing the shape memory effects inherent in multiphase metamaterials. Notably, the folded cube could bear an adult's weight (approximately 65 kg) without noticeable deformation, as shown in Fig. 8b. In contrast, a cube constructed from 3D-printed PLA polymer, although also a stiffness-variable material with the exact dimensions as the folded cube, deformed and bent under the weight of an adult because of the low stiffness. This comparison underscores the superior stiffness and strength of multiphase metamaterials, thus indicating their potential applications in various engineering domains.

We subsequently crafted a deployable structure utilizing a primitive topology with dimensions of $4 \times 4 \times 4$ unit cells (as depicted in Fig. 8c). This structure consists of LMPA encapsulated in an elastic resin. Known as a type of auxetic metamaterial with a negative Poisson's ratio [51], the primitive topology can contract laterally when subjected to a uniaxial compressive load because of the buckling deformation behavior of its ligaments. This unique contraction allows the primitive topology to form a reversibly dense structure, creating a deployable configuration. Fig. 8c illustrates the contraction of the deployable structure into a reversibly dense block when heated with boiling water. Remarkably, the volume of the deployable structure shrank by approximately 50%, from 50^3 mm^3 to 40^3 mm^3. This degree of compressibility surpasses most variable-stiffness materials, which are generally solid and incompressible. While some jamming-based materials with variable stiffness can exhibit volume compressibility, they typically demonstrate a minor stiffness change within a 100× range, as shown in Fig. 6 [38–41].

Beyond their highly adaptable stiffness, intricate geometrical topological microstructure, and excellent load-bearing capacity, multiphase metamaterials also boast the ability to form arbitrary geometries, based on the modeling method employed. These materials can be shaped into virtually any desired form using implicit functions to tune the microstructures and tailoring macroscale shapes within any boundary. Various multiphase metamaterial geometries such as hollow cylinder, torus, mushroom, and egg can be constructed using MATLAB code, commercial computer-aided design (CAD) software packages, or custom geometry generators [67,68,93], as shown in Fig. 8d. This versatility in shaping positions multiphase metamaterials as promising candidates for applications requiring complex and tailor-made forms.

4. Conclusions

In this study, we introduced a novel multiphase metamaterial inspired by TPMS topologies. Comprising up to three phases (LMPA, elastic resin, and air), these multiphase metamaterials exhibit remarkable stiffness variability of 10^5×, driven by a melting-based phase transition. The unique geometric features of the multiphase metamaterials, including bi- or tri-continuous interpenetrating microstructures, afford additional properties such as shape-memory effects, volume compressibility, and mechanical superiority as compared to other variable-stiffness materials. At room temperature, the multiphase metamaterials are highly rigid, with Young's modulus reaching into the tens of gigapascals. However, they become pliable and reconfigurable when heated above their melting temperature (approximately 82.4 °C). Notably, these materials maintain their deformed shape and automatically revert to their original form after reheating. Moreover, we presented stiffness maps of these multiphase metamaterials and explained methods to tailor their stiffness at various temperatures.

However, their fabrication is associated with certain challenges: it is difficult to use the injection molding method to create multiphase

metamaterials with submillimeter dimensions because of the surface tension of the melted alloy. To overcome this issue, multimaterial 3D printing has emerged as a promising technique for fabricating such structures using resins and LMPAs [94]. Using LMPAs and other metals with lower melting points, such as Field's metal (melting point 60 °C) and gallium (melting point 30 °C), could reduce the energy consumption required to trigger the stiffness-variable operation. Admittedly, for the metamaterials which have temperature-dependent properties, it is not easy to control in practice. Combining advanced additive manufacturing technologies, 3D-printable field-responsive smart materials, and flexible modeling methods provides a foundation for the application of multiphase metamaterials, with potential areas of use including actuators, soft robotics, shape morphing, and wearable electronics, thus highlighting the vast potential of this innovative material design.

Declaration of competing interest

The authors declare that they have no known competing financial interests or personal relationships that could have appeared to influence the work reported in this paper.

Data availability

Data will be made available on request.

Acknowledgements

This research was supported by a Grant-in-Aid for JSPS Fellows PD (Grant Number 22J11202). We acknowledge the support from the university club, Research Support, University of Tsukuba (RSUT) (https://sites.google.com/view/rs-tsukuba).

References

[1] M. Gao, Y. Meng, C. Shen, Q. Pei, Stiffness variable polymers comprising phase-changing side-chains: material syntheses and application explorations, Adv. Mater. 34 (21) (2022) 2109798.
[2] G. Lacraz, A.-J. Rouleau, V. Couture, T. Söllrald, G. Drouin, N. Veillette, M. Grandbois, G. Grenier, Increased stiffness in aged skeletal muscle impairs muscle progenitor cell proliferative activity, PLoS ONE 10 (8) (2015) e0136217.
[3] T. Sinkjaer, E. Toft, S. Andreassen, B.C. Hornemann, Muscle stiffness in human ankle dorsiflexors: intrinsic and reflex components, J. Neurophysiol. 60 (3) (1988) 1110–1121.
[4] J.R. Capadona, K. Shanmuganathan, D.J. Tyler, S.J. Rowan, C. Weder, Stimuli-responsive polymer nanocomposites inspired by the sea cucumber dermis, Science 319 (5868) (2008) 1370–1374.
[5] R. VanBuren, C.M. Wai, S. Ou, J. Pardo, D. Bryant, N. Jiang, T.C. Mockler, P. Edger, T.P. Michael, Extreme haplotype variation in the desiccation-tolerant clubmoss selaginella lepidophylla, Nat. Commun. 9 (1) (2018) 13.
[6] M. Umaña, M. Calahorro, V. Eim, C. Rosselló, S. Simal, Measurement of microstructural changes promoted by ultrasound application on plant materials with different porosity, Ultrason. Sonochem. 88 (2022) 106087.
[7] I.K. Kuder, A.F. Arrieta, W.E. Raither, P. Ermanni, Variable stiffness material and structural concepts for morphing applications, Prog. Aerosp. Sci. 63 (2013) 33–55.
[8] B. Aksoy, H. Shea, Multistable shape programming of variable-stiffness electromagnetic devices, Sci. Adv. 8 (21) (2022) eabk0543.
[9] Y. Liu, Y. Wang, X. Yang, W. Huang, Y. Zhang, X. Zhang, X. Wang, Stiffness variable polymer for soft actuators with sharp stiffness switch and fast response, ACS Appl. Mater. Interfaces (2023).
[10] M. Manti, V. Cacucciolo, M. Cianchetti, Stiffening in soft robotics: a review of the state of the art, IEEE Robot. Autom. Mag. 23 (3) (2016) 93–106.
[11] D. Rus, M.T. Tolley, Design, fabrication and control of soft robots, Nature 521 (7553) (2015) 467–475.
[12] J. Shintake, B. Schubert, S. Rosset, H. Shea, D. Floreano, Variable stiffness actuator for soft robotics using dielectric elastomer and low-melting-point alloy, in: 2015 IEEE/RSJ International Conference on Intelligent Robots and Systems (IROS), IEEE, 2015, pp. 1097–1102.
[13] T.L. Buckner, M.C. Yuen, S.Y. Kim, R. Kramer-Bottiglio, Enhanced variable stiffness and variable stretchability enabled by phase-changing particulate additives, Adv. Funct. Mater. 29 (50) (2019) 1903368.
[14] L. Blanc, A. Delchambre, P. Lambert, Flexible medical devices: review of controllable stiffness solutions, Actuators 6 (3) (2017) 23.
[15] S. Hauser, M. Robertson, A. Ijspeert, J. Paik, Jammjoint: a variable stiffness device based on granular jamming for wearable joint support, IEEE Robot. Autom. Lett. 2 (2) (2017) 849–855.
[16] S. Ling, Q. Wang, D. Zhang, Y. Zhang, X. Mu, D.L. Kaplan, M.J. Buehler, Integration of stiff graphene and tough silk for the design and fabrication of versatile electronic materials, Adv. Funct. Mater. 28 (9) (2018) 1705291.
[17] H. Du, W. Li, N. Zhang, Semi-active variable stiffness vibration control of vehicle seat suspension using an MR elastomer isolator, Smart Mater. Struct. 20 (10) (2011) 105003.
[18] S. Sun, H. Deng, H. Du, W. Li, J. Yang, G. Liu, G. Alici, T. Yan, A compact variable stiffness and damping shock absorber for vehicle suspension, IEEE/ASME Trans. Mechatron. 20 (5) (2015) 2621–2629.
[19] J.M. Jani, M. Leary, A. Subic, M.A. Gibson, A review of shape memory alloy research, applications and opportunities, Mater. Des. 56 (2014) 1078–1113.
[20] Y. Hao, J. Gao, Y. Lv, J. Liu, Low melting point alloys enabled stiffness tunable advanced materials, Adv. Funct. Mater. 32 (25) (2022) 2201942.
[21] K.M. Herbert, H.E. Fowler, J.M. McCracken, K.R. Schlafmann, J.A. Koch, T.J. White, Synthesis and alignment of liquid crystalline elastomers, Nat. Rev. Mater. 7 (1) (2022) 23–38.
[22] Y. Xia, Y. He, F. Zhang, Y. Liu, J. Leng, A review of shape memory polymers and composites: mechanisms, materials, and applications, Adv. Mater. 33 (6) (2021) 2000713.
[23] M. Herath, J. Epaarachchi, M. Islam, L. Fang, J. Leng, Light activated shape memory polymers and composites: a review, Eur. Polym. J. 136 (2020) 109912.
[24] X. Zheng, K. Uto, W.-H. Hu, T.-T. Chen, M. Naito, I. Watanabe, Reprogrammable flexible mechanical metamaterials, Appl. Mater. Today 29 (2022) 101662.
[25] W. Huang, B. Yang, L. An, C. Li, Y. Chan, Water-driven programmable polyurethane shape memory polymer: demonstration and mechanism, Appl. Phys. Lett. 86 (11) (2005) 114105.
[26] X.-J. Han, Z.-Q. Dong, M.-M. Fan, Y. Liu, J.-H. li, Y.-F. Wang, Q.-J. Yuan, B.-J. Li, S. Zhang, pH-induced shape-memory polymers, Macromol. Rapid Commun. 33 (12) (2012) 1055–1060.
[27] R. Ahamed, S.-B. Choi, M.M. Ferdaus, A state of art on magneto-rheological materials and their potential applications, J. Intell. Mater. Syst. Struct. 29 (10) (2018) 2051–2095.
[28] M.C. Yuen, R.A. Bilodeau, R.K. Kramer, Active variable stiffness fibers for multifunctional robotic fabrics, IEEE Robot. Autom. Lett. 1 (2) (2016) 708–715.
[29] S. Kamthai, R. Magaraphan, Thermal and mechanical properties of polylactic acid (PLA) and bagasse carboxymethyl cellulose (CMCB) composite by adding isosorbide diesters, in: AIP Conference Proceedings, vol. 1664, AIP Publishing LLC, 2015, p. 060006.
[30] S. Rich, S.-H. Jang, Y.-L. Park, C. Majidi, Liquid metal-conductive thermoplastic elastomer integration for low-voltage stiffness tuning, Adv. Mater. Technol. 2 (12) (2017) 1700179.
[31] D. Amoabeng, S.S. Velankar, A review of conductive polymer composites filled with low melting point metal alloys, Polym. Eng. Sci. 58 (6) (2018) 1010–1019.
[32] R. Takahashi, T.L. Sun, Y. Saruwatari, T. Kurokawa, D.R. King, J.P. Gong, Creating stiff, tough, and functional hydrogel composites with low-melting-point alloys, Adv. Mater. 30 (16) (2018) 1706885.
[33] I.M. Van Meerbeek, B.C. Mac Murray, J.W. Kim, S.S. Robinson, P.X. Zou, M.N. Silberstein, R.F. Shepherd, Morphing metal and elastomer bicontinuous foams for reversible stiffness, shape memory, and self-healing soft machines, Adv. Mater. 28 (14) (2016) 2801–2806.
[34] Y. Xin, T. Gao, J. Xu, J. Zhang, D. Wu, Transient electrically driven stiffness-changing materials from liquid metal polymer composites, ACS Appl. Mater. Interfaces 13 (42) (2021) 50392–50400.
[35] S. Chen, H.-Z. Wang, R.-Q. Zhao, W. Rao, J. Liu, Liquid metal composites, Matter 2 (6) (2020) 1446–1480.
[36] S. Mei, Y. Gao, Z. Deng, J. Liu, Thermally conductive and highly electrically resistive grease through homogeneously dispersing liquid metal droplets inside methyl silicone oil, J. Electron. Packag. 136 (1) (2014) 011009.
[37] B. Vanderborght, A. Albu-Schäffer, A. Bicchi, E. Burdet, D.G. Caldwell, R. Carloni, M. Catalano, O. Eiberger, W. Friedl, G. Ganesh, et al., Variable impedance actuators: a review, Robot. Auton. Syst. 61 (12) (2013) 1601–1614.
[38] Y. Wang, L. Li, D. Hofmann, J.E. Andrade, C. Daraio, Structured fabrics with tunable mechanical properties, Nature 596 (7871) (2021) 238–243.
[39] Y. Wang, B. Ramirez, K. Carpenter, C. Naify, D.C. Hofmann, C. Daraio, Architected lattices with adaptive energy absorption, Extreme Mech. Lett. 33 (2019) 100557.
[40] T.M. Huh, Y.-J. Park, K.-J. Cho, Design and analysis of a stiffness adjustable structure using an endoskeleton, Int. J. Precis. Eng. Manuf. 13 (2012) 1255–1258.
[41] A. Jiang, G. Xynogalas, P. Dasgupta, K. Althoefer, T. Nanayakkara, Design of a variable stiffness flexible manipulator with composite granular jamming and membrane coupling, in: 2012 IEEE/RSJ International Conference on Intelligent Robots and Systems, IEEE, 2012, pp. 2922–2927.
[42] X. Zheng, X. Zhang, T.-T. Chen, I. Watanabe, Deep learning in mechanical metamaterials: from prediction and generation to inverse design, Adv. Mater. (2023) 2302530.
[43] X. Xia, C.M. Spadaccini, J.R. Greer, Responsive materials architected in space and time, Nat. Rev. Mater. 7 (9) (2022) 683–701.

[44] X. Yu, J. Zhou, H. Liang, Z. Jiang, L. Wu, Mechanical metamaterials associated with stiffness, rigidity and compressibility: a brief review, Prog. Mater. Sci. 94 (2018) 114–173.
[45] P. Cai, C. Wang, H. Gao, X. Chen, Mechanomaterials: a rational deployment of forces and geometries in programming functional materials, Adv. Mater. 33 (46) (2021) 2007977.
[46] K. Bertoldi, V. Vitelli, J. Christensen, M. Van Hecke, Flexible mechanical metamaterials, Nat. Rev. Mater. 2 (11) (2017) 1–11.
[47] J. Qi, Z. Chen, P. Jiang, W. Hu, Y. Wang, Z. Zhao, X. Cao, S. Zhang, R. Tao, Y. Li, et al., Recent progress in active mechanical metamaterials and construction principles, Adv. Sci. 9 (1) (2022) 2102662.
[48] J. Bauer, L.R. Meza, T.A. Schaedler, R. Schwaiger, X. Zheng, L. Valdevit, Nanolattices: an emerging class of mechanical metamaterials, Adv. Mater. 29 (40) (2017) 1701850.
[49] X. Zheng, H. Lee, T.H. Weisgraber, M. Shusteff, J. DeOtte, E.B. Duoss, J.D. Kuntz, M.M. Biener, Q. Ge, J.A. Jackson, et al., Ultralight, ultrastiff mechanical metamaterials, Science 344 (6190) (2014) 1373–1377.
[50] T.A. Schaedler, A.J. Jacobsen, A. Torrents, A.E. Sorensen, J. Lian, J.R. Greer, L. Valdevit, W.B. Carter, Ultralight metallic microlattices, Science 334 (6058) (2011) 962–965.
[51] X. Zheng, X. Guo, I. Watanabe, A mathematically defined 3D auxetic metamaterial with tunable mechanical and conduction properties, Mater. Des. 198 (2021) 109313.
[52] S. Babaee, J. Shim, J.C. Weaver, E.R. Chen, N. Patel, K. Bertoldi, 3D soft metamaterials with negative Poisson's ratio, Adv. Mater. 25 (36) (2013) 5044–5049.
[53] X. Zheng, T.-T. Chen, X. Guo, S. Samitsu, I. Watanabe, Controllable inverse design of auxetic metamaterials using deep learning, Mater. Des. 211 (2021) 110178.
[54] L. Zhou, X. Zheng, K. Du, X. Guo, Q. Yin, A. Lu, Y. Yi, Parametric and experiment studies of 3D auxetic lattices based on hollow shell cuboctahedron, Smart Mater. Struct. 30 (2) (2021) 025042.
[55] X.-N. Liu, G.-K. Hu, G.-L. Huang, C.-T. Sun, An elastic metamaterial with simultaneously negative mass density and bulk modulus, Appl. Phys. Lett. 98 (25) (2011) 251907.
[56] K. Wang, J. Zhou, Q. Wang, H. Ouyang, D. Xu, Low-frequency band gaps in a metamaterial rod by negative-stiffness mechanisms: design and experimental validation, Appl. Phys. Lett. 114 (25) (2019) 251902.
[57] T. Bückmann, M. Thiel, M. Kadic, R. Schittny, M. Wegener, An elasto-mechanical unfeelability cloak made of pentamode metamaterials, Nat. Commun. 5 (1) (2014) 4130.
[58] M. Kadic, T. Bückmann, N. Stenger, M. Thiel, M. Wegener, On the practicability of pentamode mechanical metamaterials, Appl. Phys. Lett. 100 (19) (2012) 191901.
[59] J.L. Silverberg, A.A. Evans, L. McLeod, R.C. Hayward, T. Hull, C.D. Santangelo, I. Cohen, Using origami design principles to fold reprogrammable mechanical metamaterials, Science 345 (6197) (2014) 647–650.
[60] C. Coulais, D. Sounas, A. Alu, Static non-reciprocity in mechanical metamaterials, Nature 542 (7642) (2017) 461–464.
[61] X. Zheng, T.-T. Chen, X. Jiang, M. Naito, I. Watanabe, Deep-learning-based inverse design of three-dimensional architected cellular materials with the target porosity and stiffness using voxelized Voronoi lattices, Sci. Technol. Adv. Mater. 24 (1) (2023).
[62] X. Kuang, D.J. Roach, J. Wu, C.M. Hamel, Z. Ding, T. Wang, M.L. Dunn, H.J. Qi, Advances in 4D printing: materials and applications, Adv. Funct. Mater. 29 (2) (2019) 1805290.
[63] F. Momeni, X. Liu, J. Ni, et al., A review of 4D printing, Mater. Des. 122 (2017) 42–79.
[64] J.A. Jackson, M.C. Messner, N.A. Dudukovic, W.L. Smith, L. Bekker, B. Moran, A.M. Golobic, A.J. Pascall, E.B. Duoss, K.J. Loh, et al., Field responsive mechanical metamaterials, Sci. Adv. 4 (12) (2018) eaau6419.
[65] W. Zhang, J. Chen, X. Li, Y. Lu, Liquid metal-polymer microlattice metamaterials with high fracture toughness and damage recoverability, Small 16 (46) (2020) 2004190.
[66] F. Deng, Q.-K. Nguyen, P. Zhang, Multifunctional liquid metal lattice materials through hybrid design and manufacturing, Addit. Manuf. 33 (2020) 101117.
[67] O. Al-Ketan, R.K. Abu, Al-Rub, multifunctional mechanical metamaterials based on triply periodic minimal surface lattices, Adv. Eng. Mater. 21 (10) (2019) 1900524.
[68] X. Zheng, Z. Fu, K. Du, C. Wang, Y. Yi, Minimal surface designs for porous materials: from microstructures to mechanical properties, J. Mater. Sci. 53 (2018) 10194–10208.
[69] S. Kumar, S. Tan, L. Zheng, D.M. Kochmann, Inverse-designed spinodoid metamaterials, npj Comput. Mater. 6 (1) (2020) 73.
[70] L. Zheng, S. Kumar, D.M. Kochmann, Data-driven topology optimization of spinodoid metamaterials with seamlessly tunable anisotropy, Comput. Methods Appl. Mech. Eng. 383 (2021) 113894.
[71] X. Guo, X. Zheng, Y. Yang, X. Yang, Y. Yi, Mechanical behavior of TPMS-based scaffolds: a comparison between minimal surfaces and their lattice structures, SN Appl. Sci. 1 (10) (2019) 1145.
[72] S.C. Kapfer, S.T. Hyde, K. Mecke, C.H. Arns, G.E. Schröder-Turk, Minimal surface scaffold designs for tissue engineering, Biomaterials 32 (29) (2011) 6875–6882.
[73] H.-K. Liu, Y.-L. Ma, L.-J. Ren, C. Kübel, W. Wang, Symmetry and topology of twin boundaries and five-fold twin boundaries in soft crystals, Langmuir 37 (34) (2021) 10291–10297.
[74] A. Karakoç, RegionTPMS–region based triply periodic minimal surfaces (TPMS) for 3-D printed multiphase bone scaffolds with exact porosity values, SoftwareX 16 (2021) 100835.
[75] W.C. Oliver, G.M. Pharr, An improved technique for determining hardness and elastic modulus using load and displacement sensing indentation experiments, J. Mater. Res. 7 (6) (1992) 1564–1583.
[76] Metallic materials — instrumented indentation test for hardness and materials parameters, Standard ISO 14577, ISO Central Secretariat, Geneva, Switzerland, Jul. 2015.
[77] T.-T. Chen, I. Watanabe, Data-driven estimation of plastic properties in work-hardening model combining power-law and linear hardening using instrumented indentation test, Sci. Technol. Adv. Mater., Methods 2 (1) (2022) 416–424.
[78] K. Goto, I. Watanabe, T. Ohmura, Inverse estimation approach for elastoplastic properties using the load-displacement curve and pile-up topography of a single Berkovich indentation, Mater. Des. 194 (2020) 108925.
[79] I. Watanabe, A. Yamanaka, Voxel coarsening approach on image-based finite element modeling of representative volume element, Int. J. Mech. Sci. 150 (2019) 314–321.
[80] I. Watanabe, D. Setoyama, N. Nagasako, N. Iwata, K. Nakanishi, Multiscale prediction of mechanical behavior of ferrite–pearlite steel with numerical material testing, Int. J. Numer. Methods Eng. 89 (7) (2012) 829–845.
[81] W. Zhang, J. Zhou, Y. Jia, J. Chen, Y. Pu, R. Fan, F. Meng, Q. Ge, Y. Lu, Magnetoactive microlattice metamaterials with highly tunable stiffness and fast response rate, NPG Asia Mater. 15 (1) (2023) 45.
[82] M.R. Pfau, K.G. McKinzey, A.A. Roth, M.A. Grunlan, PCL-based shape memory polymer semi-IPNs: the role of miscibility in tuning the degradation rate, Biomacromolecules 21 (6) (2020) 2493–2501.
[83] L. Chen, C. Zhao, J. Huang, J. Zhou, M. Liu, Enormous-stiffness-changing polymer networks by glass transition mediated microphase separation, Nat. Commun. 13 (1) (2022) 6821.
[84] J. Peng, A.P. Tomsia, L. Jiang, B.Z. Tang, Q. Cheng, Stiff and tough PDMS-MMT layered nanocomposites visualized by AIE luminogens, Nat. Commun. 12 (1) (2021) 4539.
[85] E. Su, C. Bilici, G. Bayazit, S. Ide, O. Okay, Solvent-free UV polymerization of n-octadecyl acrylate in butyl rubber: a simple way to produce tough and smart polymeric materials at ambient temperature, ACS Appl. Mater. Interfaces 13 (18) (2021) 21786–21799.
[86] C. Bilici, V. Can, U. Nöchel, M. Behl, A. Lendlein, O. Okay, Melt-processable shape-memory hydrogels with self-healing ability of high mechanical strength, Macromolecules 49 (19) (2016) 7442–7449.
[87] Z. Zhao, S. Zhuo, R. Fang, L. Zhang, X. Zhou, Y. Xu, J. Zhang, Z. Dong, L. Jiang, M. Liu, Dual-programmable shape-morphing and self-healing organohydrogels through orthogonal supramolecular heteronetworks, Adv. Mater. 30 (51) (2018) 1804435.
[88] P. Šittner, L. Heller, J. Pilch, C. Curfs, T. Alonso, D. Favier, Young's modulus of austenite and martensite phases in superelastic NiTi wires, J. Mater. Eng. Perform. 23 (2014) 2303–2314.
[89] W. Shan, S. Diller, A. Tutcuoglu, C. Majidi, Rigidity-tuning conductive elastomer, Smart Mater. Struct. 24 (6) (2015) 065001.
[90] M.F. Ashby, L.J. Gibson, Cellular Solids: Structure and Properties, Press Syndicate of the University of Cambridge, Cambridge, UK, 1997, pp. 175–231.
[91] G.E. Fenci, N.G. Currie, Deployable structures classification: a review, Int. J. Space Struct. 32 (2) (2017) 112–130.
[92] I. Doroftei, I.A. Doroftei, Deployable structures for architectural applications-a short review, Appl. Mech. Mater. 658 (2014) 233–240.
[93] M.-T. Hsieh, L. Valdevit, Minisurf–a minimal surface generator for finite element modeling and additive manufacturing, Software Impacts 6 (2020) 100026.
[94] M.A. Skylar-Scott, J. Mueller, C.W. Visser, J.A. Lewis, Voxelated soft matter via multimaterial multinozzle 3D printing, Nature 575 (7782) (2019) 330–335.